Synthetic Metals 194 (2014) 82–87

Contents lists available at ScienceDirect

Synthetic Metals

journal homepage: www.elsevier.com/locate/synmet

The influence of the drying process on electrochemical properties of P3HT/PCBM (1.00/0.25 wt%) electrodes

L.F. Marchesi[a,b], E.C. Pereira[a,*]

[a] Laboratório de Materiais Nanoestruturados Fabricados Eletroquimicamente (Nanofael) – Universidade Federal de São Carlos, CP.: 676, DQ-UFSCar, CEP: 13565-905 São Carlos, SP, Brazil
[b] Universidade Tecnológica Federal do Paraná, Av. Monteiro Lobato s/n Km 04, CEP: 84016-210 Ponta Grossa, PR, Brazil

ARTICLE INFO

Article history:
Received 2 January 2014
Received in revised form 13 April 2014
Accepted 21 April 2014
Available online 21 May 2014

Keywords:
Polymer morphology
P3HT/PCBM electrodes
Electrochemical impedance spectroscopy

ABSTRACT

The characterization of P3HT/PCBM thin films electrodes synthesized using different drying conditions is presented in this paper. P3HT/PCBM thin film was painted on ITO substrate from a composite solution and the solvent was dried slowly, at 30 °C for 12 h, or rapidly, at 100 °C for 10 min. Atomic force microscopy data shows the formation of fibrilar-like nanostructures for the films slowly dried, behavior not observed for the films rapidly dried. The distinct morphologies had an impact on the electrochemical properties, once these electrodes containing fibrilar-like nanostructures have exhibited a better conductivity, as showed by the cyclic voltammetry response. Besides, EIS data confirms such behavior, revealing that the calculated charge transfer resistance is one order of magnitude smaller for the films slowly dried than for those quickly dried.

1. Introduction

Organic solar cells (OSC) are being intensely investigated owing to their potential to reduce production costs of solar energy, light weight and mechanical flexibility [1–4]. These systems are framed by interpenetrated nanostructures formed by a polymer donor and a fullerene acceptor acting as the active layer in a bulk-heterojunction (BHJ) solar cells [5,6]. The incident light upon the BHJ active layer, where donor and acceptor components are segregated into separated domains, gives rise to the formation of excitons that diffuse to the donor–acceptor interface, where the electron–hole charge separation occurs. Subsequently, the dissociated electrons and holes move through the percolated domains toward their corresponding electrodes, leading to the power conversion from solar energy into electric energy [7].

It is well know that morphology plays an important role in excitons separation. Considering this point, an important way to improve the device efficiency is to enhance their microstructure and/or morphology of the blend layer, which is typically amorphous due to the presence of PCBM. Thermal annealing [8,9], slow drying [10,11] and solvent annealing [12,13] have been found to be effective to restore or facilitate the polymer chain organization, resulting in PCBM segregation. Then, the formation of the donor and acceptor rich domains occurs [14–16]. Heeger et al. [17] showed that polymer solar cells with power-conversion efficiency approaching 5% and remarkable thermal stability are attained after post-production thermal annealing at 150 °C. The authors attributed the high efficiency to the thermally induced morphology modification, thermally induced crystallization and improved transport across the interface between the bulk-heterojunction material and the Al electrode. Following the same methodology, many papers showed the influence of the pre and post-annealing in BHJ solar cells [18–21]. Slowing down the drying process of the wet films leads to an enhanced blend self-organization, where the rearrangement of P3HT chains and the formation of P3HT crystallites are favored [22,23], which is expected to enhance the hole transport in P3HT [10]. As a consequence, photoconversion efficiency which exceeds 4% is observed. Mihailetchi et al. [24] using hole transport measurements, also observed the P3HT/PCBM performance enhancement when the active layer was slowly dried. The authors demonstrated that this procedure led to an increase in the hole mobility, reaching a value as large as 5.0×10^{-7} m^2 V^{-1} s^{-1} in the P3HT phase of the blend, and so, reducing the accumulation of space charges in the film. Thereat, hole–electron recombination is reduced, resulting in an increase in the photogenerated current.

Literature papers have also shown that the optical properties of P3HT/PCBM composites are strongly affected by the annealing step [25–28]. Zhokhavets et al. [29] studied the thermal annealing effect on P3HT/PCBM thin films spin coated on Si substrates. The authors concluded that thermal annealing led to an increase in the

* Corresponding author. Tel.: +55 16 3351 9309; fax: +55 16 3351 8214.
E-mail addresses: ernesto@ufscar.br, ernestopereira51@gmail.com (E.C. Pereira).

http://dx.doi.org/10.1016/j.synthmet.2014.04.018
0379-6779/

P3HT crystallinity, which resulted in a change in the P3HT optical absorption spectra peak, in the region between 2.0 and 2.5 eV, and minor changes were observed in the magnitude of the PCBM peak, in the region between 3.5 and 4.0 eV. They also observed a red shift in the P3HT peak, which was explained by an increase of the mean conjugation length of the P3HT molecules upon annealing [30–32]. Such increase in the P3HT crystallinity could be explained by the enhanced diffusion of the PCBM molecules, which allows P3HT crystallization in PCBM-free regions [33,34].

Although P3HT/PCBM systems have been extensively employed in light conversion devices, to the best of our knowledge, the influence of the drying process on the electrochemical properties of P3HT/PCBM electrodes has not been described yet in the literature, which is, in this occasion, the main purpose of this work.

2. Experimental procedure

All chemicals were of analytical grade. P3HT/PCBM composite was made adding 0.0136 g of P3HT (Sigma–Aldrich, 99%) and 0.0034 g of PCBM (Nano C, 99.5%) in 500 μL of orthodichlorobenzene (Aldrich, 99.9%). The composite was stirred in a closed vial at room temperature over 24 h prior to the electrode fabrication.

To fabricate the electrodes, indium tin oxide (ITO) substrates with an electrical resistance of 60 Ω/sq (Delta Technologies) were cleaned in ultrasonic bath with de-ionized water, acetone and methanol for 15 min, respectively. Thereafter, the composite was painted with a brush onto the substrate and the material was slowly dried in a Petri dish at 30 °C for 12 h (Sample A), or at 100 °C over 10 min (Sample B), resulting in a blend thickness very similar for both procedures (about 200 nm). The painting procedure was used instead of the large used spin coating procedure in this paper because when the blend is spin coated, part of the solvent is lost in such procedure, and the dry process study could be compromised. Painting the blends, the dry process could be more under control because the solvent lost is minimal.

Atomic force microscope (AFM) (2100 SPM microscope–Molecular Imaging) Pico LE^{TM} model operating in taping mode at a scan rate of 0.5 line/s was used for morphological characterization. Cyclic voltammetry (CV) was carried out in a three electrode cell at a scan rate of 0.020 V/s in a scan window from 0.6 V to 1.1 V. An Ag wire electrode was used as a pseudo-reference electrode, a platinum sheet electrode was used as a counter electrode and the coated P3HT/PCBM film onto ITO, as working electrode. The electrolyte was a 0.2 M $LiClO_4$ solution in acetonitrile. Electrochemical impedance spectroscopy (EIS) was carried out using the same electrochemical cell described above, polarizing the electrode in a dc potential from 0.6 V to 1.0 V, in a step of 0.1 V, with an applied ac potential of 0.01 V, in the frequency range from 10 KHz to 10 mHz. We ensured the attainment of a steady electrochemical state in the cell by waiting 5 min between the application of the dc potential and recording the data. After this period of time, the current passing through the electrochemical cell attains undetectable values. A potentiostat/galvanostat Autolab model PGSTAT30 was used for the CV and EIS experiments. Electrochemical characterization was made in the dark.

The UV–vis–NIR diffuse reflectance spectroscopy (DRS) experiments were conducted on a Varian Cary 5E UV–vis–NIR spectrophotometer attached with an integration sphere for diffuse reflectance measurements. DRS measurements was carried out in a range from 200 nm to 800 nm at room temperature and the data are presented in Kubelka–Munk plots [35].

3. Results

Fig. 1 shows AFM images of Samples A and B. One can see that different P3HT/PCBM drying process leads to changes in film morphologies. In agreement with Savenije et al. [36], the crystalline regions are characterized by plain fibrils which can be observed in Fig. 1B. These fibrilar-like regions stem from the formation of P3HT crystals from the blend film, resulting in a homogeneous distribution of fibril-like P3HT crystals within the matrix. The roughness was calculated from the AFM images and was found the values of 5.44 nm and 2.51 nm for Samples A and B, respectively. This increase in the roughness as a function of the drying process could also be related with the increase in the P3HT crystallinity, as showed by Zhao et al. [8].

The UV–vis–NIR diffuse reflectance spectroscopy (DRS) data are shown in Fig. 2. In the spectra region $E > 3.0$ eV, the absorption coefficients are mainly determined by the PCBM absorption peak at 4.0 eV. There are only minor changes in the magnitude of the PCBM peak with the dry process. The peak around 2.2 eV has been associated with π–π^* transition of P3HT [29]. The lowest absorption coefficient is observed for the sample B (fast drying) and the magnitude of the absorption coefficient increased for Sample A (dried slowly). Thus, there is a correlation between the morphology of the films and their optical absorption in the visible region of the spectrum, as we will show next. Such behavior was also showed by Savenije et al. [36], correlating morphology and crystallinity. Moreover, it is possible to estimate the P3HT/PCBM composite bandgap from the extrapolation in the x-axis of the linear spectrum part in the region of 2.0 eV. It was found that the film A has a bandgap slightly smaller than the film B (2.2 eV and 2.3 eV, respectively), also showing a correlation between morphology and bandgap [29].

Cyclic voltammetries (CV) are shown in Fig. 3. The CVs present similar characteristics, a broad oxidation peak appearing during the

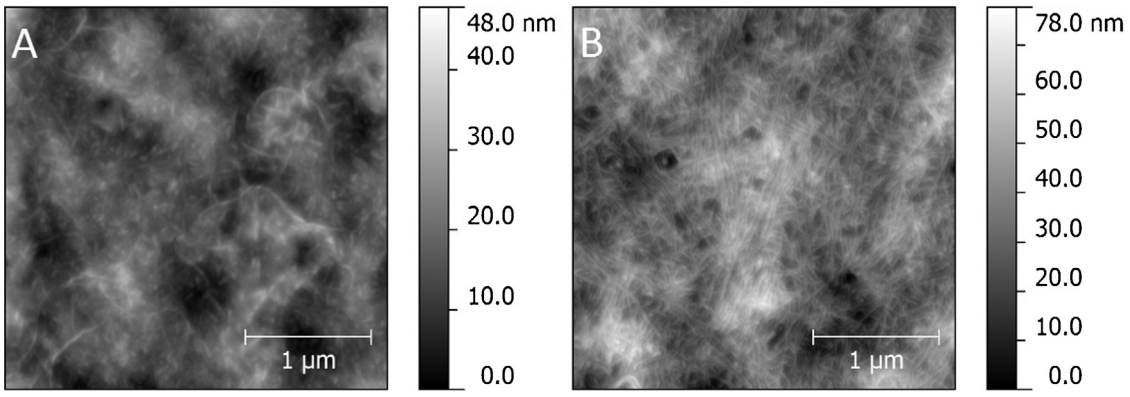

Fig. 1. AFM images of P3HT/PCBM electrodes. (a) Sample B and (b) Sample A.

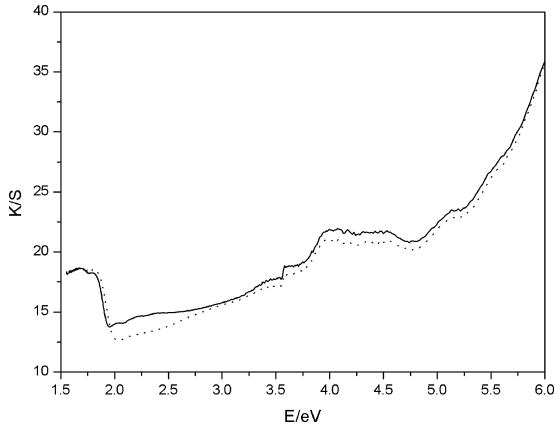

Fig. 2. UV–vis–NIR diffuse reflectance spectroscopy (DRS) data of P3HT/PCBM electrodes in Kubelka–Munk units (solid line) Sample A and (dashed line) Sample B.

positive sweep and a shifted reduction peak toward negative potentials, caused by the redox hysteresis [37], in the negative sweep. One can see that the electrochemical response is enhanced with the drying process, in other words, as the P3HT crystallinity increases, the electrochemical response increases. Besides, this behavior does not depend on the presence of PCBM, once we observed the same behavior for P3HT electrodes (not shown here).

In order to obtain information about HOMO level of the blends, the well-established equation was used:

$$E_{HOMO} = -(E_{OX} + 4.4) \ \ eV \quad (1)$$

where E_{HOMO} is the HOMO energy level, E_{OX} is the onset oxidation peak and the constant (4.4) is related to the reference electrode [38,39]. Using the bandgap values calculated from the diffuse reflectance spectroscopy (DRS), we can infer the LUMO energy level (E_{LUMO}) and the results are summarized in Table 1. One can see that the drying process affects the bandgap rising the HOMO energy level, and no displacement in the LUMO energy level was observed,

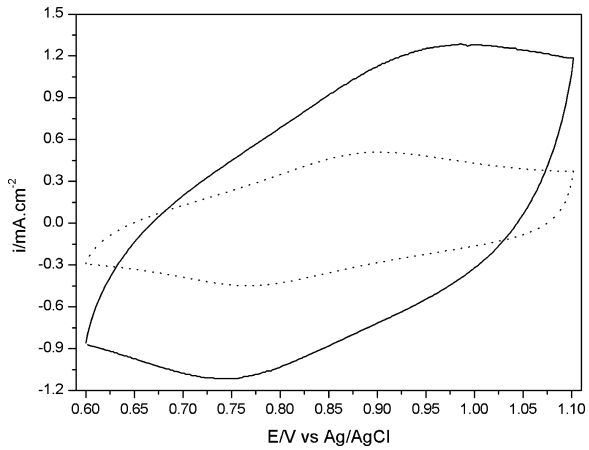

Fig. 3. Cyclic voltammograms of P3HT/PCBM electrodes performed in a scan rate of 0.02 V/s in a solution of 0.2 mol L^{-1} $LiClO_4$ in acetonitrile. Sample A (line) and Sample B (dot).

Table 1
Oxidation onset peak (E_{ox}) and the respective E_{HOMO}, E_{LUMO} and bandgap values for the P3HT and composites electrodes dried at distinct process.

Composite/dry	E_{ox}/V	E_{HOMO}/eV	E_{LUMO}/eV	Bandgap/eV
P3HT/fast	0.66	−5.1	−2.9	2.2
P3HT/slowly	0.58	−5.0	−2.9	2.1
P3HT:PCBM/fast	0.66	−5.1	−2.8	2.3
P3HT:PCBM/slowly	0.64	−5.0	−2.8	2.2

independently of the PCBM presence or not. Moreover, the rising in the HOMO energy level is also independent on the presence of the PCBM, once the displacement was 0.1 eV in both cases.

Fig. 4 shows the electrochemical impedance spectroscopy (EIS) behavior of the P3HT/PCBM film dried fast (Sample B) at several potentials from 0.6 V to 1.0 V. The EIS response has a typical

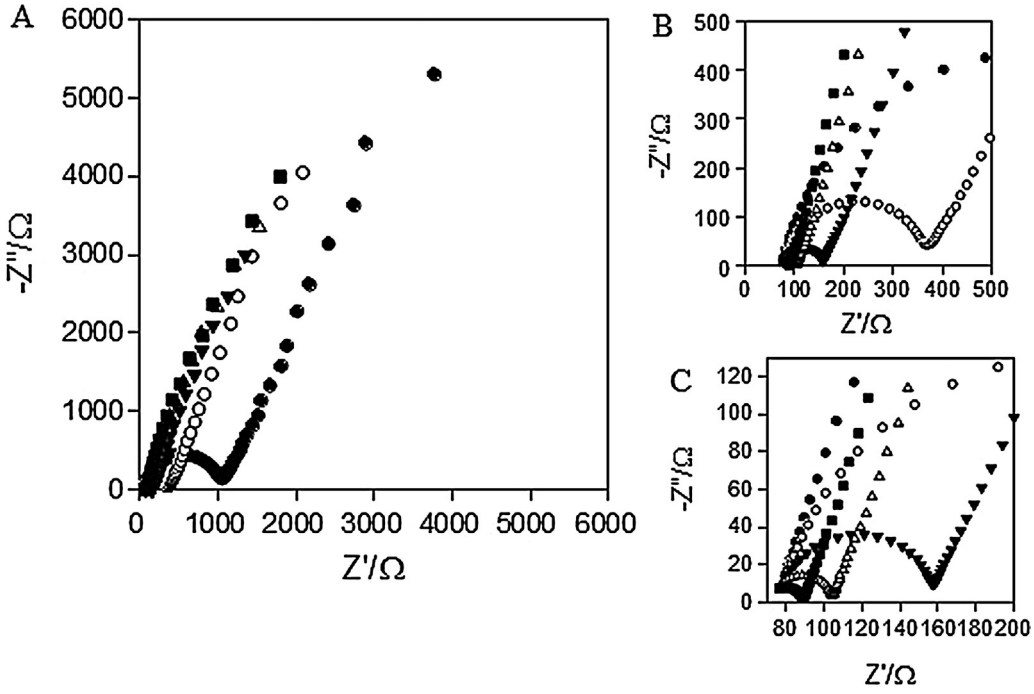

Fig. 4. EIS data of P3HT/PCBM electrodes dried fast (Sample B) carried out in 0.2 mol L^{-1} $LiClO_4$ in acetonitrile at distinct applied DC potentials from (A): (●) 0.6 V, (○) 0.7 V, (▼) 0.8 V, (Δ) 0.9 V and (■) 1.0 V. (B) and (C) high-frequency magnification.

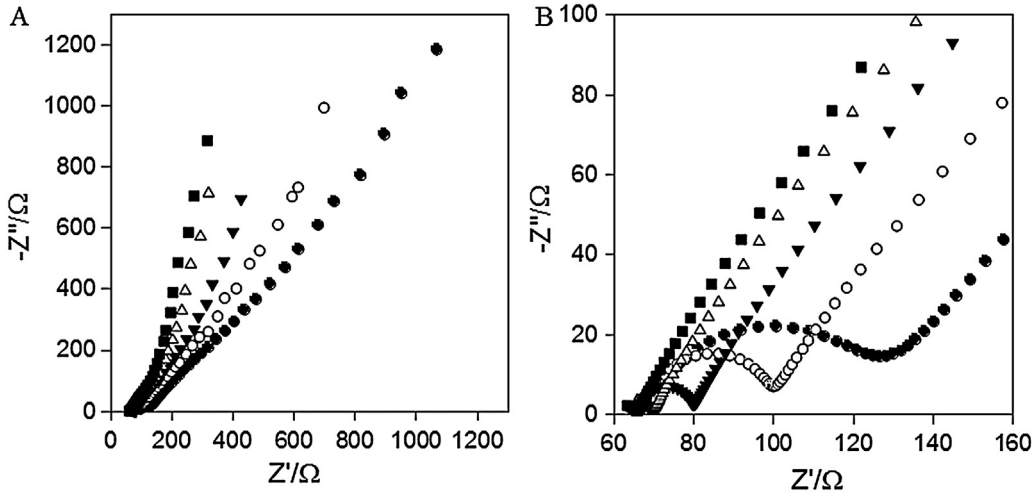

Fig. 5. EIS data of P3HT/PCBM electrodes dried slowly (Sample A) carried out in 0.2 mol L^{-1} $LiClO_4$ in acetonitrile at distinct applied DC potentials from (A): (●) 0.6 V, (○) 0.7 V, (▼) 0.8 V, (△) 0.9 V and (■) 1.0 V. (B) High-frequency magnification.

conducting polymer behavior one [40,41], that is, at high enough frequencies an arc is obtained, related to interfacial processes. The resistance of this arc is potential-dependent and is reduced as the potential reaches more positive values, evidencing the metal/insulator transition in the polymer backbone [42]. On the other hand, the low-frequency region of such plots points to the rise of capacitive behavior related to the film charging mechanism [43]. Such behavior was also observed by Hass et al. for PEDOT films [37].

In Fig. 5 are shown the EIS data for the P3HT/PCBM electrode dried slowly (Sample A). One can see the same process depicted for Sample B (a potential-dependent arc in high frequency region and a capacitive behavior in low-frequency region), additionally, one can observe a diffusion process (45° straight line) at medium frequency region, between the high-frequency arc and the low-frequency capacitance. The observation of complete diffusion impedance patterns (i.e. clear transition between Warburg- and capacitive-like behaviors) is possible in such spectra because the ionic diffusion is the actual rate-controlling factor [44]. The change in the low-frequency capacitance, as we can see by the change in the straight-line slope in the low-frequency region, is also more pronounced, which is a strong indication that the intercalation process is more evidenced in Sample A than Sample B.

The EIS data of both, Sample A and Sample B, were fitted using the appropriate equivalent circuit model, as showed in Fig. 6. It is well known that a polymeric film coated in a substrate presents a porous morphology, therewith, the more appropriate way to fit the impedance data is using the transmission line model, once this

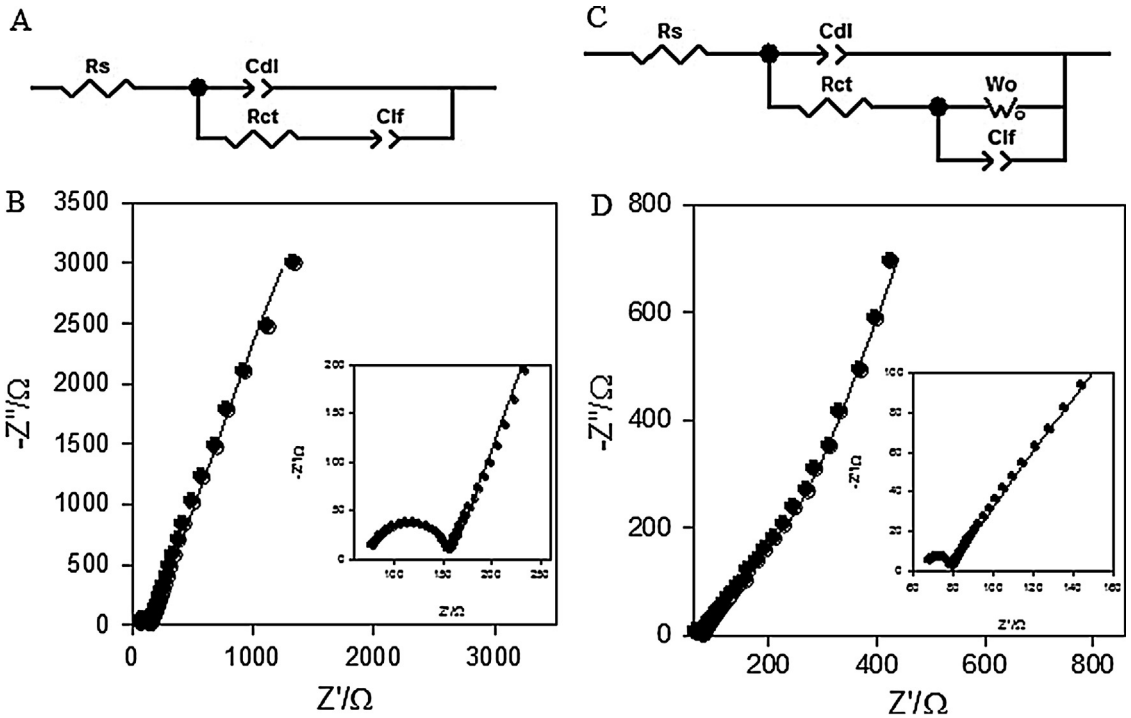

Fig. 6. Equivalent circuit model used to fit EIS data, (A) for Sample B and (C) for Sample A. EIS data obtained at 0.8 V and the fit using the respective equivalent circuit model for (B) Sample B and (D) Sample A. Inset is the high-frequency region magnification.

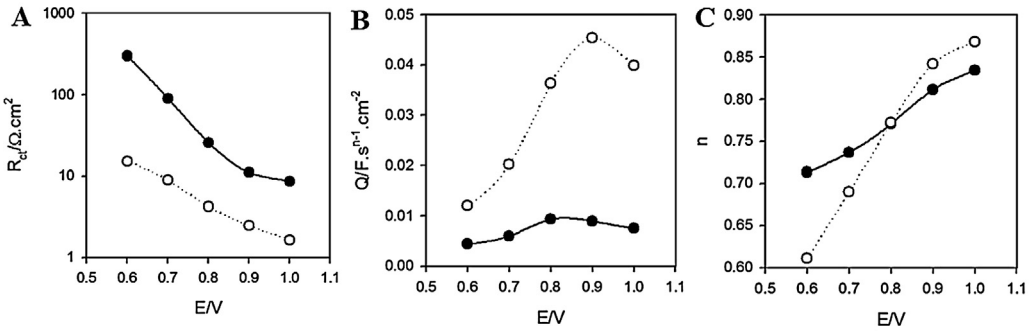

Fig. 7. (A) Charge transfer resistance, (B) low-frequency capacitance fitted with a constant phase element (CPE) and (C) CPE *n* values. (○) Sample A and (●) Sample B.

model takes into account the potential drop inside the pore and the polymeric film [40,45–48]. However, in the present case, there is no potential drop inside the film, once a straight line at high frequency region was not observed [49,50]. The equivalent circuit has a series resistance (R_S), accounting for electrolyte and contacts contribution, a capacitance accounting for the double-layer at the electrode/electrolyte interface (C_{dl}), a charge transfer resistance (R_{ct}), that represents the interfacial faradaic process, and an element accounting for the low-frequency response of the impedance data. The low-frequency response for Sample B is represented only by a capacitance element, the low-frequency capacitance (C_{lf}), related to the film charge storage (Fig. 6A). For Sample B, in addition to the low-frequency capacitance, one element representing the ionic diffusion process is also taking account, the Warburg element (W_o) (Fig. 6C) [51]. Fitting data are shown in Fig. 6B and D for Sample B and Sample A, respectively. In all cases, the capacitance elements was fitted using a constant phase element (CPE), and the regression coefficient was greater than $r^2 > 0.996$.

In Fig. 7 are shown the charge transfer resistance (R_{ct}) and the low-frequency capacitance (CPE) as a function of the applied potential. As the applied potential increase (Fig. 7A), one can see the decrease in the charge transfer resistance, reflecting the metal insulator transition. We can also observe that the values of the charge transfer resistance for Sample A are smaller than for Sample B, which is related to the dry process, showing that slowing down the velocity of the drying process, the film became more conductive, as also depicted by the CV analysis. Fig. 7B and C we can see the constant phase elements related to the low-frequency capacitance. As depicted above, this element is related to the charge film storage, once the potential applied is increase, the film became more conductive and the intercalation process of the counter-ions must occurs to guarantee charge neutrality in the film, and so, increasing the low-frequency capacitance values. We can also see that the low-frequency dependence on the applied potential is much more evidenced for Sample A (dried slowly), which could be explained by the film conductivity, once Sample A is more conductive than Sample B, more ions should be intercalated in such process. *n* can assume values from 0 to 1 and as we can see from the *Q* units, when n assumes the 1 value, *Q* recovers a perfect capacitor. As the potential is increased, the *n* values are also increased, showing that the constant phase element is becoming more capacitive as the film is oxidized. Moreover, the dependence on the applied potential of *n* is also more pronounced by Sample A than Sample B, showing that the intercalation process, and so, the charge storage, is more evidenced in Sample A.

In summary, considered the data presented here, it is possible to propose that the drying process has an important consequence in film morphology – which affects both the optical behavior and the electrochemical properties. It is also important to point out that the considerations made in this paper come from the unique (P3HT/PCBM) blend ratio used in this study (1/0.25 wt%). Any further considerations have to be provided by new experiments.

4. Conclusions

In this paper we have shown the influence of the dry process on the morphology and on both optical and electrochemical properties of P3HT/PCBM thin films. Two distinct dry processes were carried out, differing simply by the heat rates. Samples dried for 12 h at 30° (Sample A) revealed the formation of P3HT fibrilar-like nanostructures by AFM images, whilst the same morphology was not observed for those samples dried at 100 °C for 10 min (Sample B). This sort of nano architecture introduced a great impact over the conductivity for sample A, as showed by enhanced responses in CV tests, a decrease in the charge transfer resistance and an increase in the low-frequency capacitance, related to the charge storage, evaluated by EIS measurements. These fibrilar-like nanostructures also promoted increased absorption coefficients and slight changes for the P3HT bandgap, as showed by UV–vis–NIR diffuse reflectance spectroscopy.

Acknowledgements

The authors thank financial support from Fundação de Amparo à Pesquisa do Estado de São Paulo (FAPESP – 2011/19865-6), Conselho Nacional de Desenvolvimento Científico e Tecnológico (CNPq – 201380/2010-2) and Coordenação de Aperfeiçoamento de Pessoal de Nível Superior (CAPES).

References

[1] P.P. Boix, A. Guerrero, L.F. Marchesi, G. Garcia-Belmonte, J. Bisquert, Adv. Eng. Mater. 1 (2011) 1073.
[2] T.L. Andrew, V. Bulovic, ACS Nano 6 (2012) 4671.
[3] Y. He, H.Y. Chen, J. Hou, Y. Li, J. Am. Chem. Soc. 132 (2010) 1377.
[4] Y. Zhou, F. Zhang, K. Tvingstedt, S. Barrau, F. Li, W. Tian, O. Inganas, Appl. Phys. Lett. 92 (2008) 233308.
[5] Y.M. Nam, J. Huh, W.H. Jo, Sol. Energy Mater. Sol. Cells 94 (2010) 1118.
[6] H. Azimi, M. Morana, T. Ameri, B. Dastmalchi, M. Scharber, K. Hingerl, C. Brabec, Sol. Energy Mater. Sol. Cells 95 (2011) 3093.
[7] J.M. Nunzi, C. R. Physique 3 (2002) 523.
[8] Z. Zhao, L. Rice, H. Efstathiadis, P. Haldar, Microelectron. Reliab. 53 (2013) 123.
[9] M. Al-Ibrahim, O. Ambacher, S. Sensfuss, G. Gobsch, Appl. Phys. Lett. 86 (2005), 201120/1.
[10] G. Li, V. Shrotriya, J. Huang, Y. Yao, T. Moriarty, K. Emery, Nat. Mater. 4 (2005) 864.
[11] J.H. Chang, Y.H. Chen, H.W. Lin, Y.T. Lin, H.F. Meng, E.C. Chen, Org. Electron. 13 (2012) 705.
[12] Y. Zhao, Z. Xie, Y. Qu, Y. Geng, L. Wang, Appl. Phys. Lett. 90 (2007), 043504/1.
[13] G. Li, Y. Yao, H. Yang, V. Shrotriya, G. Yang, Y. Yang, Adv. Funct. Mater. 17 (2007) 1636.
[14] A. Guerrero, B. Dorling, T. Ripolles-Sanchis, M. Aghamohammadi, E. Barrena, M. Campoy-Quiles, G. Garcia-Belmonte, ACS Nano 7 (2013) 4637.

[15] M. Sanyal, B. Schmidt-Hansberg, M.F.G. Klein, C. Munuera, A. Vorobiev, A. Colsmann, P. Scharfer, U. Lemmer, W. Schabel, H. Dosch, E. Barrena, Macromolecules 44 (2011) 3795.
[16] N.D. Treat, M.A. Brady, G. Smith, M.F. Toney, E.J. Kramer, C.J. Hawker, M.L. Chabinyc, Adv. Eng. Mater. 1 (2011) 82.
[17] W. Ma, C. Yang, X. Gong, K. Lee, A.J. Heeger, Thermally stable, Adv. Funct. Mater. 15 (2005) 1617.
[18] M. Campoy-Quiles, T. Ferenczi, T. Agostinelli, P.G. Etchegoin, Y. Kim, T.D. Anthopoulos, P.N. Stavrinou, D.D.C. Bradley, J. Nelson, Nat. Mater. 7 (2008) 158.
[19] G. Garcia-Belmonte, Sol. Energy Mater. Sol. Cells 94 (2010) 2166.
[20] S. Wu, J. Li, Q. Tai, F. Yan, J. Phys. Chem. C 114 (2010) 21873.
[21] E. Verploegen, R. Mondal, C.J. Bettinger, S. Sok, M.F. Toney, Z. Bao, Adv. Funct. Mater. 20 (2010) 3519.
[22] C. Koidis, S. Logothetidis, S. Kassavetis, P.G. Karagiannidis, D. Georgiou, A. Laskarakis, Sol. Energy Mater. Sol. Cells 112 (2013) 36.
[23] A. Lange, A. Hollaender, M. Wegener, Mater. Sci. Eng. B 178 (2013) 299.
[24] V.D. Mihailetchi, H. Xie, B. de Boer, L.M. Popescu, J.C. Hummelen, P.W.M. Blom, L.J.A. Koster, Appl. Phys. Lett. 89 (2006) 012107.
[25] Y. Lu, Y. Wang, Z. Feng, Y. Ning, X. Liu, Y. Lu, Y. Hou, Synth. Met. 162 (2012) 2039.
[26] C.S. Ho, E.L. Huang, W.C. Hsu, C.S. Lee, Y.N. Lai, E.P. Yao, C.W. Wang, Synth. Met. 162 (2012) 1164.
[27] T. Erb, U. Zhokhavets, G. Gobsch, S. Raleva, B. Stuhn, P. Schilinsky, C. Waldauf, C. Brabec, Adv. Funct. Mater. 15 (2005) 1193.
[28] D. Chirvase, J. Parisi, J.C. Hummelen, V. Dyakonov, Nanotechnology 15 (2004) 1317.
[29] U. Zhokhavets, T. Erb, G. Gobsch, M. Al-Ibrahim, O. Ambacher, Chem. Phys. Lett. 418 (2006) 347.
[30] F.C. Spano, J. Chem. Phys. 122 (2005) 234701.
[31] W.J.D. Beenken, H. Lischka, J. Chem. Phys. 123 (2005) 144311.
[32] W.J.D. Beenken, T. Pullerits, J. Phys. Chem. B 108 (2004) 6164.
[33] N.D. Treat, T.E. Mates, C.J. Hawker, E.J. Kramer, M.L. Chabinyc, Macromolecules 46 (2013) 1002.
[34] K.E. Aasmundtveit, E.J. Samuelsen, M. Guldstein, C. Steinsland, O. Flornes, C. Fagermo, T.M. Seeberg, L.A.A. Petterson, O. Ingañas, R. Feidenhansl, S. Ferrer, Macromolecules 33 (2000) 3120.
[35] P. Kubelka, J. Opt. Soc. Am. 38 (1948) 448.
[36] T.J. Savenije, J.E. Kroeze, X. Yang, J. Loos, Thin Solid Films 511–512 (2006) 2.
[37] R. Hass, J. García-Cañadas, G. Garcia-Belmonte, J. Electroanal. Chem. 577 (2005) 99.
[38] F.N. Crespilho, V. Zucolotto, J.R. Siqueira, A.J.F. Carvalho, F.C. Nart, O.N. Oliveira, Int. J. Electrochem. Sci. 1 (2006) 151.
[39] J. Lohrman, C. Zhang, W. Zhang, S. Ren, Chem. Commun. 48 (2012) 8377.
[40] L.F.Q.P. Marchesi, F.R. Simões, L.A. Pocrifka, E.C. Pereira, J. Phys. Chem. B 115 (2011) 9570.
[41] F.R. Simões, L.A. Pocrifka, L.F.Q.P. Marchesi, E.C. Pereira, J. Phys. Chem. B 115 (2011) 11092.
[42] G. Garcia-Belmonte, J. Bisquert, E.C. Pereira, F. Fabregat-Santiago, J. Electroanal. Chem. 508 (2001) 48.
[43] G. Garcia-Belmonte, J. Bisquert, Electrochim. Acta 47 (2002) 4263.
[44] J. Bisquert, G. Garcia-Belmonte, A. Pitarch, ChemPhysChem 4 (2003) 287.
[45] J. Bisquert, J. Phys. Chem. B 106 (2002) 325.
[46] G. Garcia-Belmonte, J. Bisquert, E.C. Pereira, F. Fabregat-Santiago, Appl. Phys. Lett. 78 (2001) 1885.
[47] J. Bisquert, G. Garcia-Belmonte, F. Fabregat-Santiago, P.R. Bueno, J. Electroanal. Chem. 475 (1999) 152.
[48] J. Bisquert, G. Garcia-Belmonte, F. Fabregat-Santiago, A. Compte, Electrochem. Commun. 1 (1999) 429.
[49] H.S. Kim, I. Mora-Sero, V. Gonzalez-Pedro, F. Fabregat-Santiago, E.J. Juarez-Perez, N.G. Park, J. Bisquert, Nat. Commun. 4 (2013) 2242.
[50] R.G. Freitas, L.F.Q.P. Marchesi, M.R. Forim, L.O.S. Bulhões, E.C. Pereira, M.C. Santos, R.T.S. Oliveira, J. Braz. Chem. Soc. 22 (2011) 1709.
[51] J. Bisquert, G. Garcia-Belmonte, P. Bueno, E. Longo, L.O.S. Bulhões, J. Electroanal. Chem. 452 (1998) 229.